NESM- γ: An Upper-limb Exoskeleton with Compliant Actuators for Clinical Deployment

Jun Pan[1,2], *Student Member*, *IEEE*, Davide Astarita[2], Andrea Baldoni[2], Filippo Dell'Agnello[2], Simona Crea[2,3], *Member, IEEE*, Nicola Vitiello*[2,3], *Member, IEEE*, Emilio Trigili*[2], *Member, IEEE*

***Abstract*—This letter describes the design and characterization of an upper-limb exoskeleton for post-stroke rehabilitation. The platform interacts with the shoulder and elbow of the user through four active joints, driven by series elastic actuators (SEAs) with custom springs to achieve compactness and ease of maintenance. The exoskeleton adopts a passive kinematic chain for aligning the user's and robot joints' rotation axes, and a quick flipping mechanism to enable dual-side use. The pole-placement method based on the dynamic model of the SEA was used to design the low-level controller, to guarantee torque control precision and stability. The joint load due to the robot's gravity is counteracted by using a feed-forward gravity compensation algorithm. Experimental characterization demonstrates the torque control bandwidth up to 10 Hz and highly transparent behavior of the joints (namely, close to null parasitic impedance) at least up to 2 Hz, showing suitability for rehabilitation purposes.**

Index Terms—rehabilitation robotics, series elastic actuator, upper-limb exoskeleton, physical human-robot interaction

I. Introduction

The past decades have seen an emergence of prominent upper-limb rehabilitation exoskeletons [1]. Exoskeletons made of passive-compliant elements, as the soft exosuits based on cable-based transmission [2], feature low weight and inertia but relatively low control bandwidth and transmission efficiency, showing suitability mainly for the treatment of patients with low or mild movement limitations. In contrast, rigid exoskeletons with stiff structures can precisely control the power and movement between the robot and the user, potentially being able to exert sufficient torque for intensive upper-limb mobilization. Since rigid structures offer poor passive compliance, such exoskeletons must rely on active compliance to guarantee comfort during pHRI. Series-elastic actuators (SEAs) have become increasingly preferred to precisely measure and control the actuator's output torque [3].

Common implementations of SEA designs have been summarized as the *force-sensing series elastic actuator* (FSEAs), the *transmitted force-sensing series elastic actuator* (TFSEAs), and the *reaction force-sensing series elastic actuator* (RFSEAs) [4]. FSEAs place the spring between the output and the load to achieve a direct torque measurement [5], while TFSEAs utilize the gear transmission force to estimate the output torque [6]. Instead, RFSEAs place the spring between the chassis ground and the shared housing of the motor and gearbox [7]. The intermediate stage between the spring and the output equals a mechanical low-pass filter due to the gearmotor's inertia, inducing a mismatch between spring and output torque. Nevertheless, the RFSEA's spring attachment to the joint housing allows placing the compliant element either radially or axially to the transmission, facilitating a compact design. To the authors' knowledge, the Harmony [7] is the only upper-limb exoskeleton with RFSEA-based actuators. In [7], the RFSEAs were controlled by PID compensators, and a dynamic model was used for offline estimation of the joint output torque. A more detailed dynamic modeling of RFSEAs and its implementation in the low-level controller design are yet to be conducted to improve the performance.

Kinematic compatibility is another key feature that affects exoskeletons' usability. At the shoulder level, many studies [1] have applied kinematic designs with 3 degrees of freedom (DOFs) to mimic the movement of the glenohumeral (GH) joint, yet in some cases with little consideration of the additional DOFs brought by the scapulohumeral rhythm of the shoulder [8]. To mitigate the strain force at the physical human-robot interface due to poor kinematic compatibility at the scapula [9], ANYEXO [10], CLEVERarm [11], and Harmony integrated two additional active joints to preserve the scapulohumeral rhythm. Such additional DOFs require a fixed relative position of the patient's trunk with respect to the base of the shoulder mechanism due to the limited misalignment compensation. Additionally, to explore the full potential of unilateral design and maximize cost-efficacy, some devices can switch the side of use to cover a broader range of users [12]. Yet, such manual operation could be physically demanding for the operator without proper hardware or software weight relief solutions.

This work was supported in part by Regione Toscana, FAS Salute 2014 programme (call: PAR-FAS 2007-2013) under the RONDA project (RObotica indossabile personalizzata per la riabilitazioNe motoria Dell'arto superior in pAzienti neurologici), and in part by the EU Commission through the H2020 ReHyb project (Rehabilitation based on hybrid neuroprosthesis, Grant Agreement: 871767). Jun Pan was supported by the China Scholarship Council (CSC) for his study at Scuola Superiore Sant'Anna, Pisa, Italy. *Corresponding author: Jun Pan* (jun.pan@ieee.org).

*N. Vitiello and E. Trigili share the senior authorship (nicola.vitiello, emilio.trigili, @santannapisa.it).

[1]J. Pan is with the College of Mechanical Engineering, Zhejiang University of Technology, Hangzhou, Zhejiang 310023, China, and with the Key Laboratory of Special Purpose Equipment and Advanced Processing Technology, Ministry of Education and Zhejiang Province, Zhejiang University of Technology, Hangzhou, Zhejiang 310023, China.

[2]J. Pan also with D. Astarita, A. Baldoni, F. Dell'Agnello, S. Crea, N. Vitiello and E. Trigili are with The BioRobotics Institute, Scuola Superiore Sant'Anna, 56025 Pontedera, Italy, and with the Department of Excellence in Robotics & AI, Scuola Superiore Sant'Anna, 56127 Pisa, Italy.

[3]S. Crea and N. Vitiello are also with IRCCS Fondazione Don Gnocchi, Florence, 50143, Italy. They have commercial interests in IUVO S.r.l., a spinoff company of Scuola Superiore Sant'Anna. Part of the IP protecting the NESM-γ has been licensed to IUVO S.r.l. for commercial exploitation.

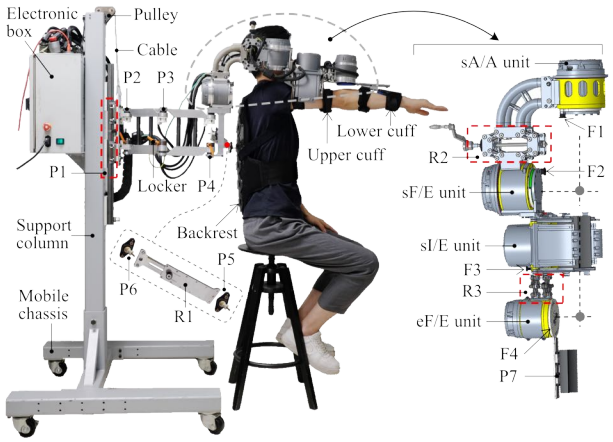

Fig. 1. Overview of the NESM-γ exoskeleton worn by a healthy subject.

This paper aims to introduce a novel upper-limb exoskeleton for rehabilitation, namely NEUROExos Shoulder-elbow Module - γ (NESM-γ), and present the preliminary experimental characterization results. The exoskeleton takes inspiration from the previous version, NESM [13], and has been upgraded with new design features, namely a kinematic chain of passive DOFs for the self-alignment of the GH joint, an actuation scheme based on RFSEA to reduce encumbrance, a differential mechanism to flip the actuation units for easy and quick dual-side use, and a model-based low-level controller. In addition to presenting the novel robot features, this paper presents the dynamic modeling, simulation, and experimental characterization of the modular RFSEA units with ad-hoc hollow springs, bringing compactness and robustness. The rest of the paper is structured as follows: Section II describes the NESM-γ mechanical structure, SEA modeling, and control system. Section III reports the experimental characterization. Finally, Section IV discusses the results and future work.

II. NESM-γ Platform

NESM-γ is a powered shoulder-elbow exoskeleton designed for the motor-function training of post-stroke patients within clinical settings (Fig. 1).

A. Mechanical Structure and Kinematics

The shoulder-elbow exoskeleton embeds four active revolute joints (Fig. 1). Three robotic joints at the shoulder address the adduction/abduction (sA/A), flexion/extension (sF/E), and intra/extra rotation (sI/E) movements of the GH joint, whereas another joint features the elbow flexion/extension movement (eF/E). The exoskeleton is mounted on a support column fixed to a wheeled platform. The column hosts the electronic box and embeds a cable-pulley mechanism with masses attached to counterweight the exoskeleton. The vertical translation via a passive slider (P1, lockable and sensorized with a potentiometer) follows the shoulder elevation/depression. The counterweight is connected to the exoskeleton through two planar links hinged in series by three passive rotational joints (P2~P4, lockable, and sensorized by encoders), allowing free translation and rotation on the horizontal plane, thus complying with the shoulder protraction/retraction and trunk rotation. Additionally, an adjustable trunk link (R1) with passive ball joints (P5, P6) at the two ends connects the back of the user and the robot, allowing for unconstrained movements of the scapula. The kinematic chain of passive DOFs (P1~P6) constitutes the self-alignment mechanism for the shoulder complex. A linear guide (P7) compensates for the potential strain on the soft tissue of the forearm due to misalignment at the elbow joint. Besides, two leadscrew-parallelogram modules (R2, R3) provide length adjustment at the upper-arm and forearm level to fit users with different upper-limb anthropometries. The weight of the movable part of the exoskeleton is about 12.8 kg.

A flipping mechanism allows the use of the device on the left or right arm by reconfiguring the range of motion (ROM) of the four active units via mechanical switches, i.e., F1~F4 (Fig. 1). The working principle of the flipping mechanism of eF/E is illustrated in Fig. 2a. Mechanical end-stop positions *a* and *b* define the joint ROM. To flip the side from left to right, the operator first opens the switch at point *c* to disengage the joint link from the SEA output, then rotates the joint link by the angle α until the switch is closed again on point *d*. The opposite sequence applies to the right-to-left flipping. The shoulder joints can be flipped by rotating the mechanical end-stop via the manual switch to reach a symmetrical fixed position without disengaging the SEA output.

The modified Denavit–Hartenberg (DH) convention is used to describe the kinematics of the robot (Fig. 2b), choosing a zero-configuration with the upper limb flexed at 90° in the sagittal plane and the palm facing downwards. The whole chain comprises three sub-chains: 1) the chain from world frame {S} to frame {O} (intersection of the three shoulder joint axes) includes four passive joints (P1~P4) for the self-alignment with the GH joint, while allowing trunk deviations; 2) the closed-loop chain O-O_{SG}-P6-P5 couples the robot and human such that the base joint J1 (sA/A) maintains a constant orientation to the human trunk (O_{SG} is the projected center of rotation (CoR) of the shoulder girdle motion), favoring the alignment between human and robotic joints during scapula motions; 3) the chain from frame {O} to frame {W} at the wrist level includes the four active units (J1~J4, Jv) and the P7 passive DOF. Jv and J3 in the third chain compose the sI/E unit, as clarified in Section II-C.

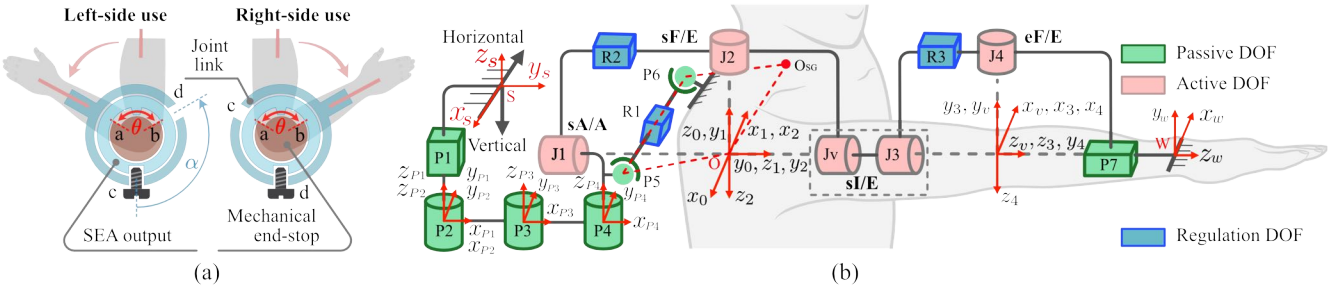

Fig. 2. (a) Quick-flipping mechanism of eF/E. (b) Kinematic chain defined by the modified DH convention, in the zero configuration.

B. SEA Units

The platform adopts a series of modular RFSEAs to actuate the joints. Here we report the technical details of the design and modeling of the SEAs.

1) Mechanical structure. Each RFSEA is driven by a brushless DC motor connected with a Harmonic Drive (HD – Limburg, Germany) gear. Notably, the sA/A and sF/E actuation units are identical, as well as sI/E and eF/E, respectively. A flat brushless DC motor (EC i-40 100w) with incremental encoder (1024 CPT, 16 EASY) from Maxon Motor (Sachseln, Switzerland) and an HD (CSD-20-160-2A-GR) are adopted for sA/A and sF/E. For sI/E and eF/E, a flat brushless DC motor (4221 BXT H 60w) with incremental encoder (IEF3-4096 L) from Faulhaber (Schönaich, Germany) and an HD (CPL-14A-100-2A) are used. Two absolute encoders (AksIM-2, RLS, Komenda, Slovenia) are adopted to measure the output torque (via the spring deformation) and position respectively. Technical data are listed in Fig. 3a.

2) *Spring design*. Custom, patented hollow springs have been designed to accommodate different torque and stiffness requirements of the anatomical joints (Fig. 3b) [14]. By housing the gearmotor inside, the hollow springs in the RFSEA reduce the axial encumbrance compared to common FSEAs, with a relatively small increase of radial encumbrance (5mm thickness). Experimental characterization demonstrates angle-torque linearity (e.g., spring in eF/E unit, Fig. 3c).

3) Dynamic modeling. Fig. 3d reports a linearized lumped-element schematic representation of the RFSEA units. The torsion spring is modeled as an inertia I_s with a stiffness of K_s, while the damping B_s considers the energy loss during spring deformation. One end of the spring is coupled to the ground chassis and the other to the motor stator inertia I_{ms}. The angle and torque inputs from the spring are θ_s and τ_s. The motor stator drives the rotor inertia I_{mr} to a position θ_m relative to the motor stator by a torque τ_m, with damping B_{sr}, accounting for the viscous friction between the motor stator and rotor. The motor is coupled to the HD by linking the motor rotor to the wave generator (WG) inertia I_{wg}, and the flexspline (FS) inertia I_{fs} to the motor stator, respectively. The input position θ_{wg} and torque τ_{wg} before the WG result in the output position θ_{fs} and torque τ_{fs} after the FS, along with the output position θ_{cs} (same as the SEA output angle θ_o) and SEA output torque τ_o, after the circular spline (CS) with inertia I_{cs}. The FS of the HD is modeled with a spring stiffness K_{fs} and a damping B_{fs}. To consider the viscous friction, we denote B_{fc}, B_{fw}, B_{cg} as the damping between: FS and CS, FS and WG, CS and chassis, respectively. $\theta_{fs}^{'}$ and $\tau_{fs}^{'}$ are the angle and output torque of the FS on the teeth side before the flexible shell of the harmonic drive. Since $K_s \ll K_{fs}$, FS approximates to a rigid body. Thus, $\theta_{fs} \approx \theta_{fs}^{'}$, $B_{fs} \approx 0$. Besides, θ_s equals θ_{fs} as the motor housing and the FS are fixed to the same base. The equations of motion for the lumped-element model are derived based on the torque balance of each inertia:

$$\begin{aligned}
I_s\ddot{\theta}_s &= -B_s\dot{\theta}_s - K_s\theta_s - \tau_s \\
I_{ms}\ddot{\theta}_s &= B_{sr}\dot{\theta}_m + \tau_s + \tau_{fs} - \tau_m \\
I_{mr}(\ddot{\theta}_m + \ddot{\theta}_s) &= -B_{sr}\dot{\theta}_m + \tau_m - \tau_{wg} \\
I_{wg}\ddot{\theta}_{wg} &= B_{fw}(\dot{\theta}_s - \dot{\theta}_{wg}) + \frac{\tau_{fs}^{'}}{N} + \tau_{wg} \\
I_{fs}\ddot{\theta}_s &= \tau_{\mathrm{fs}}^{'} - \tau_{fs} - B_{fw}(\dot{\theta}_s - \dot{\theta}_{wg}) + B_{fc}(\dot{\theta}_{cs} - \dot{\theta}_s) \\
I_{cs}\ddot{\theta}_{cs} &= -B_{fc}(\dot{\theta}_{cs} - \dot{\theta}_s) - B_{cg}\dot{\theta}_{cs} - \tau_o - \frac{N+1}{N}\tau_{fs}^{'},
\end{aligned} \tag{1}$$

where N is the catalogue gear ratio of the Harmonic Drive. The motor and gear obey the below kinematic constraints:

$$\begin{aligned}
\theta_{wg} &= (N+1)\theta_{cs} - N\theta_s \\
\theta_{wg} &= \theta_s + \theta_m.
\end{aligned} \tag{2}$$

Equations (1) and (2) show that the RFSEA is a non-homogeneous system, and the system's state can be determined only when two of the variables are under control. By taking Laplace transform of (1) and (2), we obtain:

$$\begin{aligned}
\theta_s(s) &= G_{sm}(s)\tau_m(s) + G_{sq}(s)\theta_o(s) \\
\tau_o(s) &= G_{os}(s)\theta_s(s) + G_{oq}(s)\theta_o(s),
\end{aligned} \tag{3}$$

Unit	ROM (deg)	Max torque (Nm)	Spring stiffness (Nm/rad)	HD catalogue gear ratio	Diameter × Length (mm × mm)	Weight (kg)
sA/A	0:90	25	278	160	128.5 × 125.3	2.9
sF/E	0:90	25	272	160	128.5 × 125.3	2.9
sI/E	-88:28	10	184	100	104 × 107	1.8
eF/E	-120:0	10	190	100	90.5 × 111.8	1.4

(a)

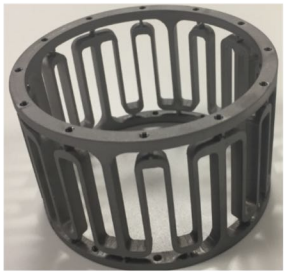

(b)

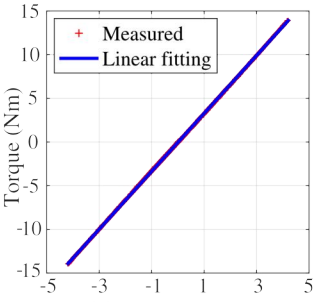

(c)

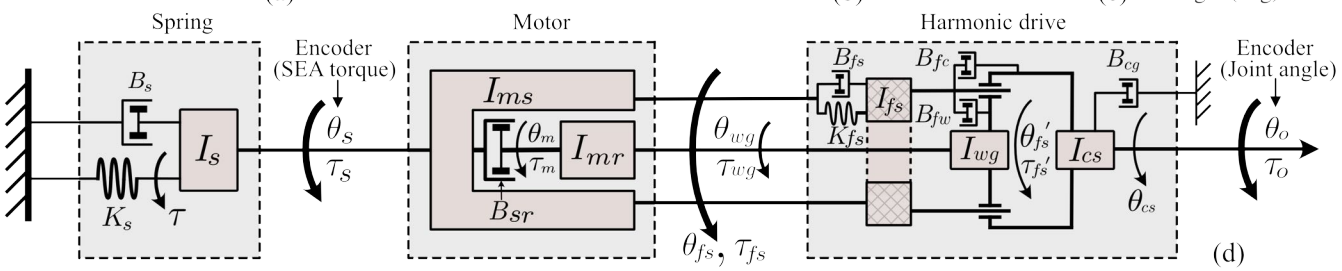

(d)

Fig. 3. RFSEA unit: (a) technical data of the SEA units; (b) torsion spring; (c) spring characterization for eF/E unit; (d) lumped-element linear model.

where:

$$G_{sm}(s) = \frac{-N-1}{(N^2 I_M + I_S)s^2 + \big((N+1)^2 B_F + B_{fc} + B_s\big)s + K_s}$$

$$G_{sq}(s) = \frac{N(N+1)I_M s^2 + \big((N+1)^2 B_F + B_{fc}\big)s}{(N^2 I_M + I_S)s^2 + \big((N+1)^2 B_F + B_{fc} + B_s\big)s + K_s}$$

$$G_{os}(s) = (NI_M - I_S)s^2 - B_s s - K_s$$

$$G_{oq}(s) = -\big((N+1)I_M + I_{cs}\big)s^2 - B_{cg}s,$$

and $I_M = I_{wg} + I_{mr}$; $B_F = B_{fw} + B_{sr}$; $I_S = I_{fs} + I_s + I_{ms}$.

Assuming that the spring inertia I_s and damping B_s are negligible in (1), the measured spring torque $\tau(s)$ can be regarded as equal to $\tau_s(s)$, i.e.,

$$\tau(s) = -K_s\theta_s(s) \approx \tau_s(s). \tag{4}$$

Equation (3) shows the open-loop transfer function of the system. $\tau_o(s)$ in (3) has a different form from $\tau(s)$ in (4) since the RFSEA does not place the torque sensor (i.e., spring) on the output. We assume that the approximation of the measured spring torque to the actual output torque holds in the low-frequency band, which is then verified in Section III-A.

C. Differential mechanism of the sI/E joint

The sI/E unit integrates a geared differential mechanism to divert power transmission by 90° (Fig. 4). Such mechanism directly mobilizes humeral rotation and has a wide and symmetrical ROM (i.e. 116 deg) for both the left and right sides of use.

The SEA housing is attached to the planet carrier, and the output shaft directly drives the sun gear (z_4 teeth). Two planet bevel gears (z_3 teeth) engage with the sun gear and transmit the power to the proximal and distal ring gears (z_1 teeth) by two spur gears (z_2 teeth). The proximal ring gear is fixed to the upstream robotic link (its output is blocked) and interfaces the arm through the upper cuff, while the distal ring gear interfaces the eF/E unit and then couples with the forearm through the lower cuff. The relative rotation between the two ring gears is thus transferred to the arm. The kinematic constraints are modeled as:

$$\frac{\omega_o}{\omega_e - \omega_c} = z, \quad \frac{\omega_o}{\omega_p - \omega_c} = -z, \quad \omega_p = 0, \tag{5}$$

where $z = \frac{z_1 z_3}{z_2 z_4}$. ω_e and ω_p are the angular velocities of the distal and proximal ring gears, respectively, ω_c is the velocity of the planet carrier around the limb axis, ω_o is the output velocity of the SEA. From (5) we obtain the gear ratio from SEA output to planet carrier (SEA housing) as:

$$\frac{\omega_o}{\omega_c} = z, \tag{6}$$

and the gear ratio from SEA output to distal ring gear as:

$$r_t = \frac{\omega_o}{\omega_e} = \frac{z}{2}. \tag{7}$$

Since the differential mechanism exhibits three different motions (ω_e, ω_p *and* ω_c), we added a virtual DH joint Jv at the coupling point of the proximal ring gear to describe the motion of the planet carrier (see in Fig. 2b and Fig. 4). Both the gravity load of the virtual DH link G_c on Jv and the external load τ_e on J3 are driven by the same SEA unit but with different transmission ratios (see (6) and (7)). Therefore, we obtain the required SEA output torque as:

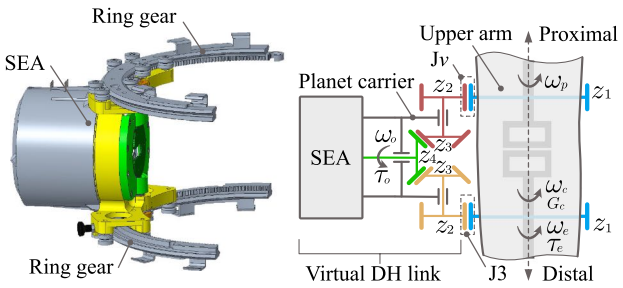

Fig. 4. Differential mechanism of sI/E unit: CAD model (left) and its kinematic coupling with the upper arm (right).

$$\tau_o = -\frac{G_c}{z} - \frac{2\tau_e}{z}. \tag{8}$$

D. Gravity compensation

We model the gravity balance of a single joint in its local coordinate frame, as shown in Fig. 5. The gravity torque on each joint results from the contributions of the latter robotic links in the kinematic chain. Therefore, the gravity torque vector applied to a joint can be calculated as follows:

$$\begin{aligned} \boldsymbol{G}_j &= \sum_{k=j}^{4} \boldsymbol{r}_k^j \times m_k \boldsymbol{g}_j \\ &= \big[G_{xj}\ G_{yj}\ G_{zj}\big]^T, \quad \forall j \in [1,2,v,3,4], \end{aligned} \tag{9}$$

where:

$$\boldsymbol{g}_j = R_{j0}\boldsymbol{g}_0, \qquad \begin{bmatrix} \boldsymbol{r}_k^j \\ 1 \end{bmatrix} = T_{jk} \begin{bmatrix} \boldsymbol{r}_k^k \\ 1 \end{bmatrix},$$

and $\boldsymbol{r}_k^j$ is the position vector of the center of mass m_k of link k in the joint frame $\{j\}$. $\boldsymbol{g}_j$ is the gravity vector in frame $\{j\}$ with $\boldsymbol{g}_0 = [0,0,-g]^T$. G_{xj}, G_{yj}, G_{zj} are the components of torque applied by gravity about the three axes of frame $\{j\}$. R_{j0} is the rotation matrix that orients world frame $\{O\}$ to joint frame $\{j\}$. T_{jk} transforms joint frame $\{k\}$ to $\{j\}$. R_{j0} and T_{jk} are calculated using the DH model defined in Fig. 2b.

SEAs of sA/A, sF/E, and eF/E have direct actuation; thus, $-G_{zj}$ is the SEA torque required for gravity balance. However, since sI/E integrates a differential mechanism, its gravity compensation torque should be calculated according to (8), where $G_c = G_{zv} - G_{z3}$, $\tau_e = G_{z3}$. Thus, we obtain the gravity compensation torques for all the four SEAs:

$$\tau_{Gj} = \begin{cases} -G_{zj}, & \text{if } j = 1,2,4 \\ \dfrac{-G_{zv} - G_{z3}}{z}, & \text{if } j = 3 \end{cases}. \tag{10}$$

The calculation of (10) requires the determination of mass (m_k and m_v) and center of mass ($\boldsymbol{r}_k^k$ *and* $\boldsymbol{r}_v^v$) information. These parameters were identified using the experimental procedure described in [15], which was proven more accurate than estimations based on CAD drawings.

E. Control system

The control system features a hierarchical architecture that comprises a high-level control layer (HLCL) and a low-level control layer (LLCL), as in Fig. 6. HLCL executes user-

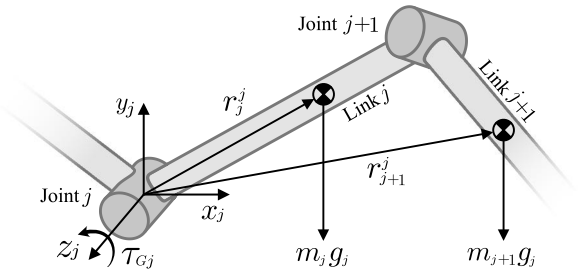

Fig. 5. Gravity balance model of a single joint.

commanded decisions (i.e., desired interaction torques) and feeds the real-time control objectives (i.e., reference torque) to LLCL, while LLCL takes the control input and outputs the right current to the motor driver to track the reference variable.

1) High-level control layer: The NESM- γ control system grounds on the so-called patient-in-charge control modality, which refers to the operation of the joints in torque-control mode. Using this control scheme, the robot either remains "transparent" to the user's movements or can selectively provide joint torques (or a desired variable impedance) to assist or resist the user's movement, enabling the treatment of patients with a wide range of movement abilities. A feed-forward gravity compensation algorithm is implemented based on (10) to compensate for the torques due to the exoskeleton's weight. The desired torque commanded to the low-level controller is the sum of the pose-dependent gravity compensation torque (τ_{Gj}) and a torque reference (τ_{hj}). τ_{hj} is computed by the high-level control layer according to the interaction strategy adopted (i.e., $\tau_{hj} = 0$ enables the transparent mode). For the sI/E joint, the multiplication with r_t (or $1/r_t$) considers the effect of the differential mechanism on the torque (or position), where r_t is the gear ratio from (7).

2) Low-level control layer: The design of the controller is based on the identification of the open-loop transfer function of the system. The model for the identification is obtained by simplifying (3). Observing the weighting factors of the parameters in (3), we can neglect I_S, I_{cs} and B_{fc} due to their low impact on the equation. B_s can also be ignored since the spring is made of metal with low damping values. Besides, B_{cg} is close to zero since the ball bearing has low viscous friction [16]. Consequently, finding the explicit expression of the open-loop system in (3) only relies on identifying two parameters, i.e., I_M and B_F. The identification was performed via open-loop tests against the mechanical stop (set $\theta_o(s) = 0$), by commanding chirp signals of motor current ($i_m^{'}$) with different amplitudes and frequencies as the input and measuring the spring torque $\tau(s)'$ as output. The commanded motor torque was approximated as $\tau_m^{'} = k_c i_m^{'}$, where k_c is the torque constant. Therefore, with (2), (3) and (4), the open-loop transfer function for the identification test is given as:

TABLE I. TRANSFER FUNCTIONS FOR PERFORMANCE EVALUATION

	Torque tracking ($\theta_o = 0$)	**Transparency** ($\tau_d = 0$)
Spring	$\frac{\tau(s)}{\tau_d(s)} = \frac{K_s C(s) G_{sm}(s)}{K_s C(s) G_{sm}(s) - 1}$	$\frac{\tau(s)}{\theta_o(s)} = \frac{K_s G_{sq}}{K_s C(s) G_{sm}(s) - 1}$
Actual output	$\frac{\tau_o(s)}{\tau_d(s)} = -\frac{G_{os}(s)}{K_s} \cdot \frac{\tau(s)}{\tau_d(s)}$	$\frac{\tau_o(s)}{\theta_o(s)} = -\frac{G_{os}(s)}{K_s} \cdot \frac{\tau(s)}{\theta_o(s)} + G_{oq}(s)$

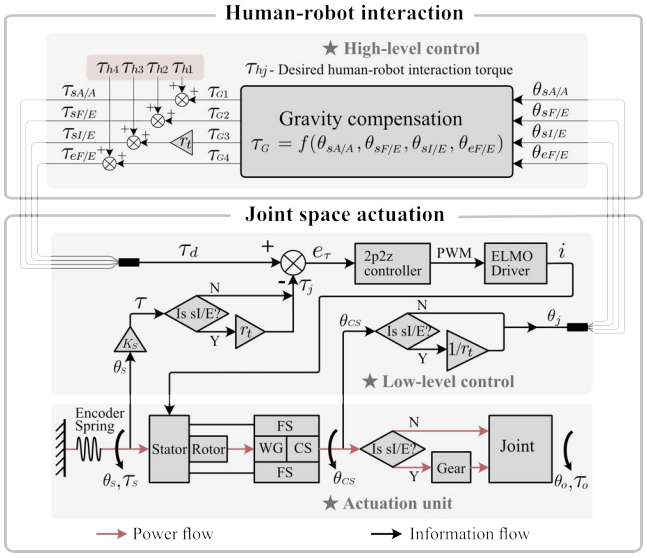

Fig. 6. Patient-in-charge control scheme.

$$\frac{\tau(s)^{'}}{\tau_m^{'}} = \frac{K_s(N+1)}{N^2 I_M s^2 + (N+1)^2 B_F s + K_s}. \qquad (11)$$

Based on the identified model, a 2-pole-2-zero (2p2z) controller $C(s)$ was designed with the pole-placement method, with an integrator term to nullify the steady-state error, a high-frequency pole (a_1) to bound the overshoot due to the high band noise, one zero (b_1) to enforce the settling time of the response and a second zero (b_2) as a stabilizing action. To evaluate the RFSEA performance, the transfer functions for the torque tracking (with output blocked, $\theta_o = 0$) and transparency analysis (in terms of output impedance when a null interaction torque is commanded, $\tau_d = 0$) are formulated as shown in TABLE I, considering both the spring torque and the output load torque. The low-level closed-loop system is schematized in Fig. 7.

F. *Hardware control unit*

The hardware control unit comprises a real-time controller, sbRIO-9651 (National Instruments—NI, Austin, TX, USA), endowed with a Xilinx Zynq-7020 System on Chip. A 667-MHz dual-core ARM Cortex-A9 processor runs a NI real-time operating system and a Field Programmable Gate Array (FPGA) unit Xilinx Artix-7. The HLCL runs at 100 Hz on the real-time unit, whereas the LLCL runs at 1 kHz on the FPGA.

III. EXPERIMENTS AND RESULTS

In this section, we first report the simulation results of the torque tracking and transparency performance based on the identified open-loop system, and estimate the bandwidth that guarantees a good approximation between the measured spring torque and actual output torque. Then, the characterization of the low-level torque control of the actuation unit(s) is presented. We reported both a single-joint (eF/E) bench test and the evaluation of the multi-joint mobilization to assess the

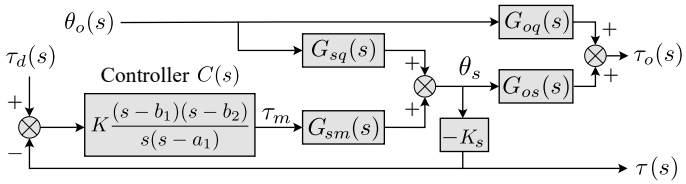

Fig. 7. Block diagram of low-level closed-loop system.

reliability of our RFSEA implementation and the performance of the low-level torque controller.

A. Simulation results

By calculating the transfer functions in TABLE I, we obtain the simulated torque tracking and transparency performance of the eF/E unit as shown in Fig. 8a, where the impedance is normalized to the spring stiffness for a fair comparison among actuators of different stiffnesses. The torque tracking Bode plots (blue lines) show a deviation of amplitudes between the torque measured by the spring and the estimated SEA output torque lower than 10% up to 21.4 Hz. The output impedance for spring and SEA output (green curves) increases with higher frequencies and tends to match the spring stiffness in both cases. The difference between the two amplitude plots is lower than 10% under 22.2 Hz.

B. Characterization of the single-joint performance

1) Step response. The responsiveness of the torque controller was evaluated by analyzing the step response. To hold the joint output locked, a torque offset was set to push it against the mechanical stop. Then, positive and negative steps at different amplitudes (from 2 to 5 Nm) were fed as desired input to the controller, and the spring torque was measured. Fig. 8b plots the measured torque averaged across three trials. A maximum overshoot of 10.3% and rising time (10% to 90% of the steady-state value) smaller than 0.05 s ensure good reactiveness of the controller and reliability of the hardware.

2) Chirp response. One chirp torque reference signal with an amplitude of 1 Nm was commanded, with the joint output locked, covering a frequency range from 0.01 to 10 Hz. Results in Fig. 8c show almost a null difference of the measured torque from the desired value at around 0.1 Hz and an error of 13.4% at 10 Hz with a phase lag of 71.5° (Fig. 8d). The maximum amplitude deviation between the theoretical and experimental Bode plots is 1.24 dB. Both plots do not reach -3dB amplitude before 10 Hz, demonstrating that the system can provide torques precisely and efficiently in the human frequency range [17].

3) Output impedance. A healthy subject wearing the exoskeleton performed an elbow flexion/extension with an amplitude > 60°, while the robot was in transparent mode. The subject was asked to follow a metronome set at an increasing frequency from 0.2 Hz to 2 Hz, and four repeated trials were executed. The controller's performance was evaluated through parasitic torques measured by the SEA spring during the movement. The torque slightly overcomes 1 Nm only near 2 Hz (Fig. 8e). Averaged Bode plot over all the trials (Fig. 8f) shows that the measured amplitude of normalized impedance deviates from the simulation by a maximum of 11.8% within 2 Hz. The measured impedance is -43.1 dB at 2 Hz.

C. Characterization of Multi-joint Performance

Five healthy subjects (2 females, 3 males) were recruited to characterize the multi-joint performance. The subjects signed informed consent before participation. Two functional movements, i.e., circle tracking and water pouring, were performed with the exoskeleton in transparent mode to evaluate the general transparency of the four active joints. The movements were chosen to reproduce typical ADL tasks (i.e., circular wiping and point-to-point reaching) that covers different task spaces in the frontal and horizontal planes.

1) Circle tracking. Each subject was asked to move the fist along a circle (136 mm radius) printed on a vertical board. All subjects started with the arm in a fixed pose (sA/A at 90°, sF/E at 60°, sI/E at 0°, eF/E at -70°) and the fist aligned with the circle center. The test involved three trials with different speeds expressed in beats per minute (bpm), i.e., 22 bpm, 32 bpm, 42 bpm, paced by a metronome. For each trial, 12 repetitions were performed. Before starting the trial, the subject rested the fist on the 12 o'clock position.

2) Water pouring. The subject held a cup to simulate water pouring movement on a table about 150 mm lower than the chest. A target position was marked on the table, 300 mm from the chest and 150 mm from the sagittal plane. The subject performed the water pouring task starting with the arm in a fixed pose (sA/A, sF/E at 90°, sI/E at 0°, eF/E at -90°), between

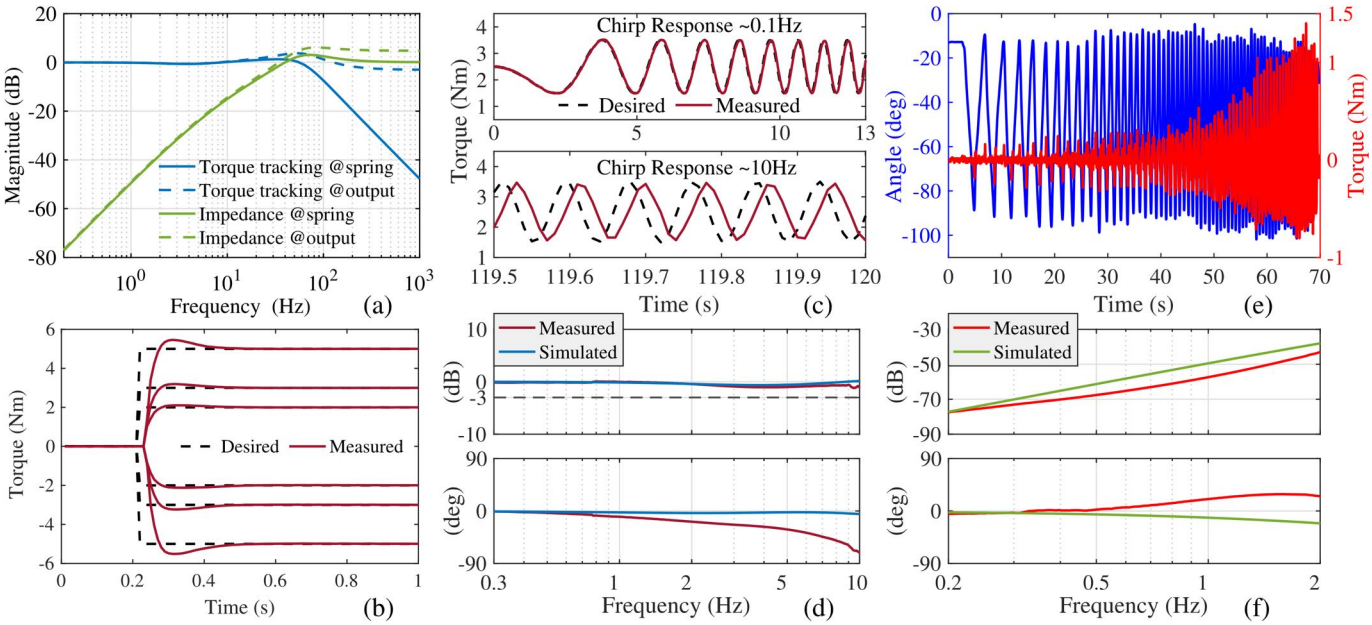

Fig. 8. Characterization result of the eF/E unit. (a) Simulation results of torque tracking and normalized impedance. (b) Step response test. (c) Torque tracking performance. (d) Closed loop bandwidth. (e) Raw data of the impedance test. (f) Bode diagram of the amplitude and phase of the normalized joint impedance.

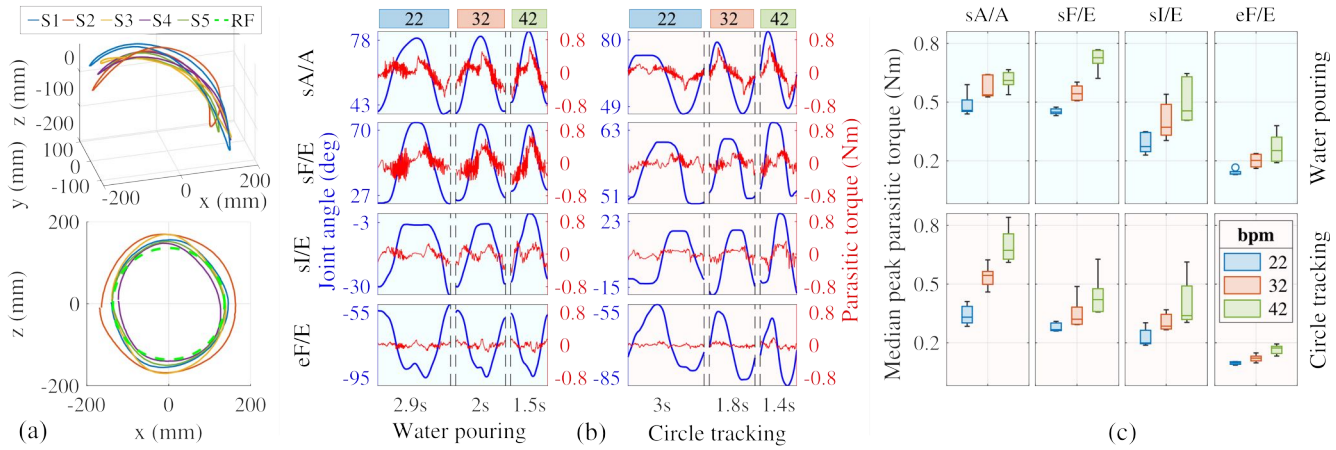

Fig. 9. (a) End effector trajectory of the water pouring task and (up) circle tracking task (down), S1 to S5 are the actual hand trajectories of the subjects, RF is the reference trajectory (only for the circle trcking). (b) Parasitic torque and joint angle of one cycle duration under three speeds (22, 32,42 bpm) for water pouring (left) and circle tracking movement (right). (c) Statistics of the median peak parasitic torque of the two functional movements across all subjects.

the zero and target positions, back and forth for 12 repetitions. The same speeds as the circle tracking task were tested.

The end effector trajectories of each subject (i.e., approximated hand trajectories, Fig. 9a) were calculated for both tasks using the DH model. Data were segmented into individual movement cycles by finding the peaks of the azimuth angle of the end-effector trajectory in cylindrical coordinates. The last ten repetitions of each task were processed. We evaluated the transparency of the actuation units as the parasitic torque of the joints when the system was set in "transparent" mode. The parasitic torque was calculated as the net torque delivered to the human joint, i.e., the difference between the measured spring torque τ_j and the gravity compensation torque τ_{Gj} calculated by (10), disregarding the inertia of the robotic link. The positive and negative peaks of the parasitic torque were then obtained within each cycle. We further extracted the local top 5% torque values around the peaks to calculate each speed's absolute median peak torque. One representative data cycle of each trial is visualized in Fig. 9b for both tasks. The distribution of this torque across all subjects is shown in Fig. 9c. Higher speed leads to greater median peak torque for all four joints and both tasks, in line with the simulation results in Fig. 8(a). Additionally, sA/A and sF/E joints with higher payload exhibit higher median peak torque than the other two joints, due to the bigger inertia and damping friction of the SEA components.

IV. Discussion and Conclusion

This letter reported the development of a shoulder-elbow exoskeleton for post-stroke robot-assisted therapy that satisfies two requirements. First, from the therapist's perspective, the robot should be reconfigurable efficiently to either side of use and should not require demanding adaptation of the patient to the robot. Second, from the patient's perspective, the robot should provide high-fidelity torque control that endows precise torque tracking ability and high transparency, with a bandwidth high enough to enable multiple training modalities (active-assistive, active, and resistive [18]) that rely on precise and timely torque delivery. Furthermore, in a post-stroke rehabilitation scenario, a high torque-control bandwidth would be beneficial to deal safely with sudden, unpredicted movements, e.g., muscle spasticity [13].

We developed a flipping mechanism to allow a therapist to change the side of use of the robot easily and quickly (around 1 minute), while the robot is set in transparent mode with gravity compensation, demanding a minimal physical effort from the operator. Armin III [19] shows a comparable flipping functionality, but only with motors powered off during operation. A similar approach was adopted by ChARMin [12], which involved an additional toggling operation of the passive gravity compensation mechanism. Besides, NESM-γ integrated a passive kinematic chain to preserve scapulohumeral rhythm by auto-aligning the CoRs of the robotic and GH joint. Different from other solutions with powered joints, such chain facilitates the donning procedure without the need of restricting the user's trunk with respect to the robot for proper alignment. Although powered designs can actively assist scapulohumeral rhythm and behave similarly to the passive ones when operated in transparent mode, we chose passive DOFs to reduce the overall complexity from mechatronic and control perspectives.

Moreover, a differential mechanism was adopted to mobilize the sI/E unit, reducing hysteresis issues existing in "motor-belt" transmission [20] and exhibiting a bigger ROM than traditional "motor-gear" solutions of the same dimension [21] (the design doubles the relative rotation between the distal and proximal ends). The sI/E unit directly measures the position of humeral rotation and human-robot interaction torque, without the need for theoretical estimations as in other shoulder designs with series-chain of revolute joints that lack joint-by-joint human-robot correspondence [7], [11].

The RFSEA-based architecture has been designed to achieve precise torque control for NESM-γ due to its compactness and robustness. A detailed dynamical model of the RFSEA was developed to investigate the theoretical approximation between the torque measured via the spring deformation and the actual output torque. We believe that such a theoretical framework will be valuable for the design and development of novel RFSEA-based exoskeletons, as well as to simulate more advanced low-level control strategies for SEAs. Both simulation results of the torque tracking and the output impedance confirm that under 21.4 Hz, the approximation of the spring torque to the SEA output torque holds. Meanwhile, the good fitting between the simulation and actual results verifies the accuracy of the dynamic model of

the RFSEA. Besides, NESM-γ characterization showed a bandwidth higher than 10 Hz and a normalized output impedance of -43.1 dB at 2 Hz, outperforming the 6.9 Hz and -25 dB at 1 Hz of the previous version [13]. Limitations of the tests arise due to current saturation at the driver level; thus, frequencies higher than 10 Hz could not be investigated to find the resonance frequency. Nevertheless, higher bandwidth is not mandatory in a rehabilitation context, where relatively slow mobilizations are performed. Other recent SEA-based shoulder-elbow exoskeletons are the Harmony [7] and the ANYexo [10]. The RFSEAs of NESM-γ differ from Harmony's in that the former assigns the CS of the harmonic drive as the output, while the latter's output is the FS, resulting in different dynamic models. Harmony can withstand a torque of 34.4 Nm at the shoulder and 13 Nm at the elbow (>NESM-γ) in a bandwidth of 7 Hz (<NESM-γ). As an RFSEA-based actuation, the approximation between the measured spring torque and the actual output torque was verified up to around 15.9 Hz (<NESM-γ). ANYexo can provide 40 Nm peak torque at a bandwidth higher than 60 Hz at 3 Nm amplitude, exhibiting better performance than NESM-γ, thanks to the more powerful motors (240/720 W) than the ones (50/100 W) in NESM-γ. While ANYexo was conceived to develop control algorithms and hardware concepts in a laboratory environment (as stated by the authors), NESM-γ targets a balanced tradeoff between performance and usability for both patients and therapists to facilitate the daily use in the actual clinical setting.

Transparent behavior was achieved via a model-based low-level torque controller with feed-forward gravity compensation and was experimentally evaluated to verify suitability for training ADLs. As expected, the functional movements exhibited higher residual torques and inter-subject variability with increasing movement speed levels, due to the lack of feed-forward friction and inertia compensation in the SEAs. Such effects were higher for sA/A and sF/E due to the higher payload of these joints. Nevertheless, for "slow" movements (22 bpm, i.e., about 0.3 Hz) [13], which are more comparable to the ones expected in a post-stroke rehabilitation session, the residual torques were below 0.5 Nm for all joints. The performance of the gravity compensation is comparable to the closed-loop controller adopted in ARMin IV+ [22], owing to an accurate gravity model and high-fidelity torque control of the actuators. Also, NESM-γ relies on torque sensors integrated within SEA-based joints, while ARMin IV+ depends on the multi-axis force/torque sensors installed at the pHRI points. The former has good precision and high efficiency in executing joint space tasks, approximating the interaction with anatomical joints when a proper compensation of the disturbances is applied. Conversely, the latter maps the force/torque from the sensors onto the robotic joints by Jacobian matrix, which is computationally less efficient but better controls Cartesian-space tasks.

In the future, we strive to investigate the friction's effect on the torque control to improve the system's transparency. Experimental characterization of the shoulder passive kinematic chain will be performed to assess its impact on shoulder muscles and kinematics. This would pave the way for the clinical validation of the device to prove its effectiveness in the recovery of motor functions of post-stroke patients.

REFERENCES

[1] N. Rehmat, J. Zuo, W. Meng, Q. Liu, S. Q. Xie, and H. Liang, "Upper limb rehabilitation using robotic exoskeleton systems: a systematic review," *Int. J. Intell. Robot. Appl.*, vol. 2, no. 3, pp. 283–295, Sep. 2018.

[2] H. Majidi Fard Vatan, S. Nefti-Meziani, S. Davis, Z. Saffari, and H. El-Hussieny, "A review: A Comprehensive Review of Soft and Rigid Wearable Rehabilitation and Assistive Devices with a Focus on the Shoulder Joint," *J. Intell. Robot. Syst.*, vol. 102, no. 1, p. 9, May 2021.

[3] A. J. Veale and S. Q. Xie, "Towards compliant and wearable robotic orthoses: A review of current and emerging actuator technologies," *Med. Eng. Phys.*, vol. 38, no. 4, pp. 317–325, Apr. 2016.

[4] C. Lee, S. Kwak, J. Kwak, and S. Oh, "Generalization of Series Elastic Actuator Configurations and Dynamic Behavior Comparison," *Actuators*, vol. 6, no. 3, p. 26, Aug. 2017.

[5] F. Giovacchini *et al.*, "A light-weight active orthosis for hip movement assistance," *Robot. Auton. Syst.*, vol. 73, pp. 123–134, Nov. 2015.

[6] M. Lauria and M.-A. Legault, "Differential Elastic Actuator for Robotic Interaction Tasks," *IEEE Int. Conf. Robot. Autom.*, p. 6, 2008.

[7] B. Kim and A. D. Deshpande, "An upper-body rehabilitation exoskeleton harmony with an anatomical shoulder mechanism: design, modeling, control, and performance evaluation," *Int. J. Robot. Res.*, vol. 36, no. 4, pp. 414–435, Apr. 2017.

[8] J. Crosbie, S. L. Kilbreath, L. Hollmann, and S. York, "Scapulohumeral rhythm and associated spinal motion," *Clin. Biomech.*, vol. 23, no. 2, pp. 184–192, Feb. 2008

[9] A. H. A. Stienen, E. E. G. Hekman, F. C. T. van der Helm, and H. van der Kooij, "Self-Aligning Exoskeleton Axes Through Decoupling of Joint Rotations and Translations," *IEEE Trans. Robot.*, vol. 25, no. 3, pp. 628–633, Jun. 2009.

[10] Y. Zimmermann, A. Forino, R. Riener, and M. Hutter, "ANYexo: A Versatile and Dynamic Upper-Limb Rehabilitation Robot," *IEEE Robot. Autom. Lett.*, vol. 4, no. 4, pp. 3649–3656, Oct. 2019.

[11] A. Zeiaee, R. Soltani Zarrin, A. Eib, R. Langari, and R. Tafreshi, "CLEVERarm: A Lightweight and Compact Exoskeleton for Upper-limb Rehabilitation," *IEEE Robot. Autom. Lett.*, pp. 1–1, 2021.

[12] U. Keller, H. J. A. van Hedel, V. Klamroth-Marganska, and R. Riener, "ChARMin: the first actuated exoskeleton robot for pediatric arm rehabilitation," *IEEE/ASME Trans. Mechatron.*, vol. 21, no. 5, pp. 2201–2213, Oct. 2016.

[13] E. Trigili *et al.*, "Design and Experimental Characterization of a Shoulder-Elbow Exoskeleton With Compliant Joints for Post-Stroke Rehabilitation," *IEEE/ASME Trans. Mechatron.*, vol. 24, no. 4, pp. 1485–1496, Aug. 2019.

[14] N. Vitiello, F. Giovacchini, A. Baldoni, and M. Cempini, "Joint for transmitting a torsional load with elastic response," WO2017216740A1, Dec. 21, 2017.

[15] S. Moubarak, M. T. Pham, R. Moreau, and T. Redarce, "Gravity compensation of an upper extremity exoskeleton," *Annu. Int. Conf. IEEE Eng. Med. and Biol.*, 2010, pp. 4489–4493.

[16] M. Bălan, L. Houpert, A. Tufescu, and D. Olaru, "Rolling Friction Torque in Ball-Race Contacts Operating in Mixed Lubrication Conditions," *Lubricants*, vol. 3, no. 2, pp. 222–243, Apr. 2015.

[17] T. L. Brooks, "Telerobotic response requirements," *IEEE Int. Conf. Syst., Man, Cybern.*, 1990, pp. 113–120.

[18] S. Dalla Gasperina, L. Roveda, A. Pedrocchi, F. Braghin, and M. Gandolla, "Review on Patient-Cooperative Control Strategies for Upper-Limb Rehabilitation Exoskeletons," *Front. Robot. AI*, vol. 8, p. 745018, Dec. 2021.

[19] T. Nef, M. Guidali, and R. Riener, "ARMin III – arm therapy exoskeleton with an ergonomic shoulder actuation," *Appl. Bionics Biomech.*, vol. 6, no. 2, pp. 127–142, Jul. 2009.

[20] Y. Shen, J. Ma, B. Dobkin, and J. Rosen, "Asymmetric Dual Arm Approach For Post Stroke Recovery Of Motor Functions Utilizing The EXO-UL8 Exoskeleton System: A Pilot Study," *Annu. Int. Conf. IEEE Eng. Med. and Biol.*, 2018, pp. 1701–1707.

[21] M. H. Rahman, M. J. Rahman, O. L. Cristobal, M. Saad, J. P. Kenné, and P. S. Archambault, "Development of a whole arm wearable robotic exoskeleton for rehabilitation and to assist upper limb movements," *Robotica*, vol. 33, no. 1, pp. 19–39, Jan. 2015.

[22] F. Just *et al.*, "Exoskeleton transparency: feed-forward compensation vs. disturbance observer," - *Autom.*, vol. 66, no. 12, pp. 1014–1026, Dec. 2018.